Identification of the permeability field of a porous medium from the injection of a passive tracer

Lang Zhan and Yannis C. Yortsos
Petroleum Engineering Program, Department of Chemical Engineering, University of Southern California, Los Angeles, California 90089-1211

(Received 27 September 1999; revised manuscript received 28 February 2000)

We propose a method for the direct inversion of the permeability field of a porous medium from the analysis of the displacement of a passive tracer. By monitoring the displacement front at successive time intervals (for example, using a tomographic method), the permeability can be directly obtained from the solution of a nonlinear boundary-value problem. Well posedness requires knowledge of the pressure profile or the permeability at no-flow boundaries. The method is tested using synthetic data in two dimensions (2D) (and some 3D) geometries for a variety of heterogeneous fields and found to work well when the permeability contrast is not too large. However, it is sensitive to sharp variations in permeability. In the latter case, a modified approach based on the successive injection in both directions and the use of an optimization technique leads to improved estimates. The sensitivity to measurement errors is analyzed. An important feature of the direct method is that it also applies to anisotropic porous media. When the principal axes of anisotropy are known, a suitable procedure is proposed and demonstrated using synthetic data.

PACS number(s): 47.55.Mh, 46.65.+g, 05.40.−a, 05.60.−k

I. INTRODUCTION

Permeability heterogeneity is a most important feature of natural porous media, as it affects significantly flow and fluid displacement properties. These dictate flow paths, and the migration and dispersion of *in situ* or injected fluids in porous media, with applications ranging from the recovery of *in situ* fluids to the fate of environmental contaminants in the subsurface [1]. Heterogeneity is manifested at various scales, from the laboratory (core) to the megascopic (field) scale. Its ubiquitous and multiscale nature has attracted the interest of many investigators, and a variety of studies have been devoted to its characterization and identification [2].

The classical approach for identifying permeability heterogeneity is based on the inversion of pressure data, under single-phase flow conditions [3]. Given that the transient flow of slightly compressible fluids in porous media obeys the diffusion equation, a variety of field tests (well tests) have been devised to infer permeability features by matching pressure data at well locations to the solution of the diffusion equation. Pressure transient methods have also been applied to characterize the heterogeneity of laboratory cores, using minipermeameters [4]. These devices essentially conduct miniwell tests on the surface of a laboratory core (by injecting a small pulse of air and monitoring the resulting pressure transient), which are used to infer a map of the permeability heterogeneity at the external surface of the sample.

An alternative approach to permeability identification is based on the analysis of the arrival times during the injection of passive tracers (namely of tracers which do not affect the fluid viscosity and density). Various efforts have been made at the field scale to relate the arrival times to the permeability, and to match assumed permeability fields to such data [5]. These techniques are usually indirect, based on optimizing arbitrary (or constrained) initial guesses to match data at various, usually sparse, locations. As a result, they suffer from nonuniqueness. Nonetheless, useful information can be extracted, which can be used to constrain images of the subsurface permeability field.

When knowledge of the displacement front at successive time intervals is available, for example, through visual or tomographic techniques, arrival time methods should in principle be able to provide direct maps of the heterogeneity. Brock and Orr [6] reported one such attempt, based on the visualization of displacements in a two-dimensional (2D) heterogeneous bead pack. Withjack *et al.* [7] proposed a model to infer the permeability heterogeneity of laboratory samples from the analysis of concentration contours obtained from x-ray computerized tomography (CT). Their model is based on a number of simplifying assumptions, the main of which is that each flow streamtube has constant (but unknown) permeability and porosity, which is thus tantamount to an assumption of a layered structure. Although restrictive, the work of Withjack *et al.* [7] was the first to point out the potential of CT in identifying the permeability heterogeneity. CT techniques are now routinely applied to monitor displacement fronts in porous media at the laboratory scale. Advances in field scale tomography, for example, by seismic methods or cross-hole tomography, are also likely to lead to analogous results at the field scale [8]. Yet, well-defined methods to invert such information to determine the permeability heterogeneity are currently lacking.

In this paper, we propose a method that focuses on this question, namely, on how to invert data on arrival times at various (and numerous) points in the porous medium to map the permeability field. The method, elements of which were briefly described in Ref. [9], is based on a direct inversion of the data, rather than on the optimization of initial random (or partly constrained) guesses of the permeability field. It is based on two basic premises, that Darcy's law for single-phase flow in porous media is valid, and that the dispersion of the concentration of the injected tracer is negligible. Based on these conditions, we formulate a nonlinear boundary value problem, the coefficients of which depend on the experimental arrival time data. Combined with informa-

tion on the permeability or the pressure at the bounding (no-flow) surface of the porous medium we obtain a solution of the boundary-value problem, from which the permeability field can be directly calculated. The requirement that pressure or permeability values at a boundary must be known makes the method more suitable to laboratory applications. An important feature of the method is that it can be applied to determine the heterogeneity of anisotropic media, where the permeability field is a tensor, as is often the case in many natural porous media. For this, displacements in two (for 2D) or three (for 3D) different directions must be conducted.

As described below, the experimental information on arrival times enters in the technique in the form of spatial derivatives. As a result, the solution method is sensitive to errors in their estimation, which are expected to increase when variations in the permeability are sharper and larger. The errors are magnified around certain limiting streamlines, the width of which increases in the downstream direction, and may lead to poor estimates of the permeability in some regions. To circumvent the problem in such cases, we have modified the inversion method by considering a forth-and-back hybrid approach, in which arrival times are recorded a second time by repeating the tracer displacement in the reverse direction. This approach is then combined with an optimization technique to improve the resulting estimates. The need to repeat the displacement in two directions in such cases, may be an additional limitation on the applicability of the method to field cases.

The paper is organized as follows. In Sec. II we describe the inversion method for the case of isotropic media. Section III shows numerical examples which test the applicability of the method to various forms of permeability heterogeneity and its sensitivity to permeability variation and spatial correlation. Section IV describes the hybrid approach for inverting permeability fields with sharp and large contrasts. A sensitivity study of the effect of measurement errors is also provided. The extension of the method to anisotropic media of known and fixed principal axes is presented in Sec. V. We close with concluding remarks.

II. DIRECT INVERSION ALGORITHM: ISOTROPIC MEDIA

Consider the injection of a passive tracer in a heterogeneous and isotropic porous medium. In the absence of dispersion, the concentration $C(\mathbf{x},t)$ satisfies the equation

$$\phi(\mathbf{x})\frac{\partial C}{\partial t}+\mathbf{v}\cdot\nabla C=0, \tag{1}$$

where $\phi(x)$ is the porosity of the medium and $\mathbf{v}$ is the superficial fluid velocity vector. Under slow, viscous flow conditions, the latter satisfies Darcy's law

$$\mathbf{v}=-\mathbf{K}\cdot\nabla\Phi \tag{2}$$

and the continuity equation

$$\nabla\cdot\mathbf{v}=0 \tag{3}$$

assuming incompressible fluids. Here, $\mathbf{K}(x)$ is the (symmetric) permeability tensor, and Φ is a flow potential, $\nabla\Phi=(1/\mu)(\nabla p-\rho\mathbf{g})$, where μ is viscosity, taken as a constant, p is pressure, ρ is density, also assumed constant, and $\mathbf{g}$ is the acceleration of gravity. For isotropic media we take $\mathbf{K}(x)=k(\mathbf{x})I$, where $\mathbf{I}$ is the identity tensor. The anisotropic case is discussed in Sec. V. In the absence of dispersion, we define a front location by the equation

$$\mathcal{F}(\mathbf{x},t)\equiv t-f(\mathbf{x})=0, \tag{4}$$

where, assuming constant or monotonic injection rates, the function $f(\mathbf{x})$ is single valued, thus associated with a given point $\mathbf{x}$ is a single arrival time. Then, the concentration is given by

$$C(x,t)=C_i(t)H(t-f(\mathbf{x})), \tag{5}$$

where $C_i(t)$ is the injection concentration and H is the Heaviside step function.

The direct algorithm is based on the following. First, we equate the two expressions for the normal velocity at the front, given by the kinematics and by Darcy's law, respectively. Noting that the normal at the front is given by

$$\mathbf{n}=\frac{\nabla\mathcal{F}}{|\nabla\mathcal{F}|}=-\frac{\nabla f}{|\nabla f|}, \tag{6}$$

we combine Eqs. (5) and (6) with Eq. (1) to obtain a kinematic expression for the normal velocity there, namely,

$$v_n=-\frac{\phi(\mathbf{x})}{|\nabla f|}. \tag{7}$$

Darcy's law [Eqs. (2) and (6)] gives another expression for the same quantity

$$v_n=\frac{k(\mathbf{x})\nabla\Phi\cdot\nabla f}{|\nabla f|}. \tag{8}$$

From Eqs. (7) and (8) we obtain the following result for the permeability:

$$k(\mathbf{x})=-\frac{\phi(\mathbf{x})}{\nabla\Phi\cdot\nabla f} \tag{9}$$

which, in principle, can be evaluated in terms of Φ and f. Substituting the above expression in Darcy's law and making use of the continuity equation (3) we obtain a nonlinear equation for Φ, which reads

$$\nabla\cdot\left[\frac{\phi(\mathbf{x})\nabla\Phi}{\nabla\Phi\cdot\nabla f}\right]=0. \tag{10}$$

The two equations (9) and (10) constitute the keys of the direct inversion method. Equation (10) is a partial differential equation which determines Φ, given appropriate boundary conditions, and information on the porosity $\phi(\mathbf{x})$ and the arrival time function $f(\mathbf{x})$. From its solution, the permeability field can be directly calculated using Eq. (9).

The following remarks are in order.

(1) For the solution of Eq. (10), the porosity must be a known function of the spatial coordinates. For applications using CT, this is readily available.

(2) Although, at first glance, Eq. (10) appears to be an elliptic (Laplace type) equation, it is in fact a system of first-order hyperbolic equations. This can be readily shown, e.g., in 2D, by introducing

$$u \equiv \frac{\partial \Phi / \partial y}{\partial \Phi / \partial x} \tag{11}$$

in which case Eq. (10) becomes

$$\frac{\partial}{\partial x}\left[\frac{\phi(\mathbf{x})}{f_x + u f_y}\right] + \frac{\partial}{\partial y}\left[\frac{\phi(\mathbf{x}) u}{f_x + u f_y}\right] = 0, \tag{12}$$

where subscripts indicate partial derivatives. (A similar analysis holds for 3D.) The two Eqs. (11) and (12) form a pair of first-order hyperbolic equations. For their solution, and thus for the solution of Eq. (10), information on the potential Φ at the (no-flow) boundaries is necessary. Equivalently, this information can be furnished from a knowledge of the permeability at the boundaries (which, for instance, can be obtained for a laboratory sample by a minipermeameter, as previously noted). At no-flow boundaries (where in the normal direction $\partial \Phi / \partial n = 0$), Eq. (9) becomes a partial differential equation for the variation of Φ along the boundary, which can be integrated, given k and f at the boundary, to yield the required profile. In this way, the numerical method utilizes information from all boundaries, essentially solving an ellipticlike, rather than a hyperbolic system. In the applications to be shown below we solved Eq. (10) assuming pressure profiles are known at all boundaries.

(3) A notable feature of Eqs. (9) and (10) is that they depend on the gradient of the front arrival time rather than on the arrival time itself. On the positive side, this reflects a desirable sensitivity of the method to heterogeneity. However, this dependence also introduces numerical instability which can lead to problems when the permeability contrast is sharp and large. A technique to circumvent these problems and its sensitivity to error in measurements is described later in Sec. IV.

In summary, supplied with boundary conditions on the potential, Eqs. (9) and (10) can be solved directly to yield the permeability field in a heterogeneous porous medium based on information on arrival times and the porosity heterogeneity. The resolution of the inverted permeability field depends, among others, on the resolution of the arrival time contours.

Stream-function approach for 2D *geometries*. Before proceeding, it is worthwhile to note that in 2D geometries, an alternative inversion method is possible, based on the use of the stream function Ψ, where $\partial \Psi / \partial y = v_x$ and $\partial \Psi / \partial x = -v_y$. Stream-function-based methods were proposed by Brock and Orr [6] and Withjack *et al.* [7], using Heuristic arguments, as noted previously. To proceed with such an approach, we first rearrange Eq. (7) to read

$$\frac{\partial f}{\partial y}\frac{\partial \Psi}{\partial x} - \frac{\partial f}{\partial x}\frac{\partial \Psi}{\partial y} = -\phi(\mathbf{x}). \tag{13}$$

This is a first-order, hyperbolic differential equation for Ψ, the characteristics of which are curves of constant f, namely, of constant arrival time, which are available experimentally. Hence, the stream function can be computed by integrating along these contours, for example,

$$\Psi = \Psi_0 + \int_{y_0}^{y} \frac{\phi}{f_x} dy, \tag{14}$$

where, in the case of a rectilinear sample with a no-flow boundary at $y_0 = 0$, we can take $\Psi_0 = 0$ without loss. To estimate the permeability we also need to compute the potential. In the isotropic case, we make use of the fact that equipotentials are orthogonal to the streamlines, thus

$$\frac{\partial \Psi}{\partial x}\frac{\partial \Phi}{\partial x} + \frac{\partial \Psi}{\partial y}\frac{\partial \Phi}{\partial y} = 0. \tag{15}$$

Equation (15) is also a hyperbolic equation, which can be integrated subject to appropriate boundary conditions. Then, the permeability can be estimated from Eq. (9), or from the alternative expression $k = \partial \Psi / \partial y / \partial \Phi / \partial x$. This approach does not rely on the restrictive approximations made by the previous authors. Illustrative examples will be discussed below.

III. APPLICATIONS USING SIMULATED DATA

The direct inversion method was subsequently tested based on simulated data. We used a high-resolution finite-difference simulator (the main features of which are described in Ref. [10]), or a streamline-based method, to simulate tracer displacement at constant-rate and in the absence of gravity and provide data on arrival times and the pressure profile at the boundaries. Parenthetically, we note that the forward problem belongs to the general class of problems recently discussed by Sethian [11], and can also benefit from the application of a fast marching technique. Such was not implemented here, however. The numerical results thus obtained, were considered ''error-free'' data to be used as input for the solution of Eq. (10). The boundary value problem (10) was solved using a standard SOR finite-difference formalism, which was suitably iterated until convergence. For example, for the 2D geometry we used the five-point scheme

$$\begin{aligned} &\Theta^m_{i+1/2,j}\Phi^{m+1}_{i+1,j} + \Theta^m_{i-1/2,j}\Phi^{m+1}_{i-1,j} + \Theta^m_{i,j+1/2}\Phi^{m+1}_{i,j+1} \\ &\quad + \Theta^m_{i,j-1/2}\Phi^{m+1}_{i,j-1} - (\Theta^m_{i+1/2,j} + \Theta^m_{i-1/2,j} + \Theta^m_{i,j+1/2} \\ &\quad + \Theta^m_{i,j-1/2})\Phi^{m+1}_{i,j} = 0, \end{aligned} \tag{16}$$

where $\Theta^m_{i,j}$ is the conductivity coefficient at block (i,j) at iteration level m. All other coefficients were evaluated using the harmonic average between $\Theta^m_{i,j}$ and its nearest neighbor. An interpolation routine was used to interpolate the arrival times, when necessary. The spatial derivatives of f were calculated using three-point differences. Equation (16) was solved using prescribed pressure profiles on the two no-flow boundaries.

Figures 1–3 show results of the application of the inversion method in three 2D heterogeneity fields of a moderate permeability contrast, corresponding to a layered medium, a medium with a smoothly varying heterogeneity and a permeability distribution following the FBM (fractional Brownian

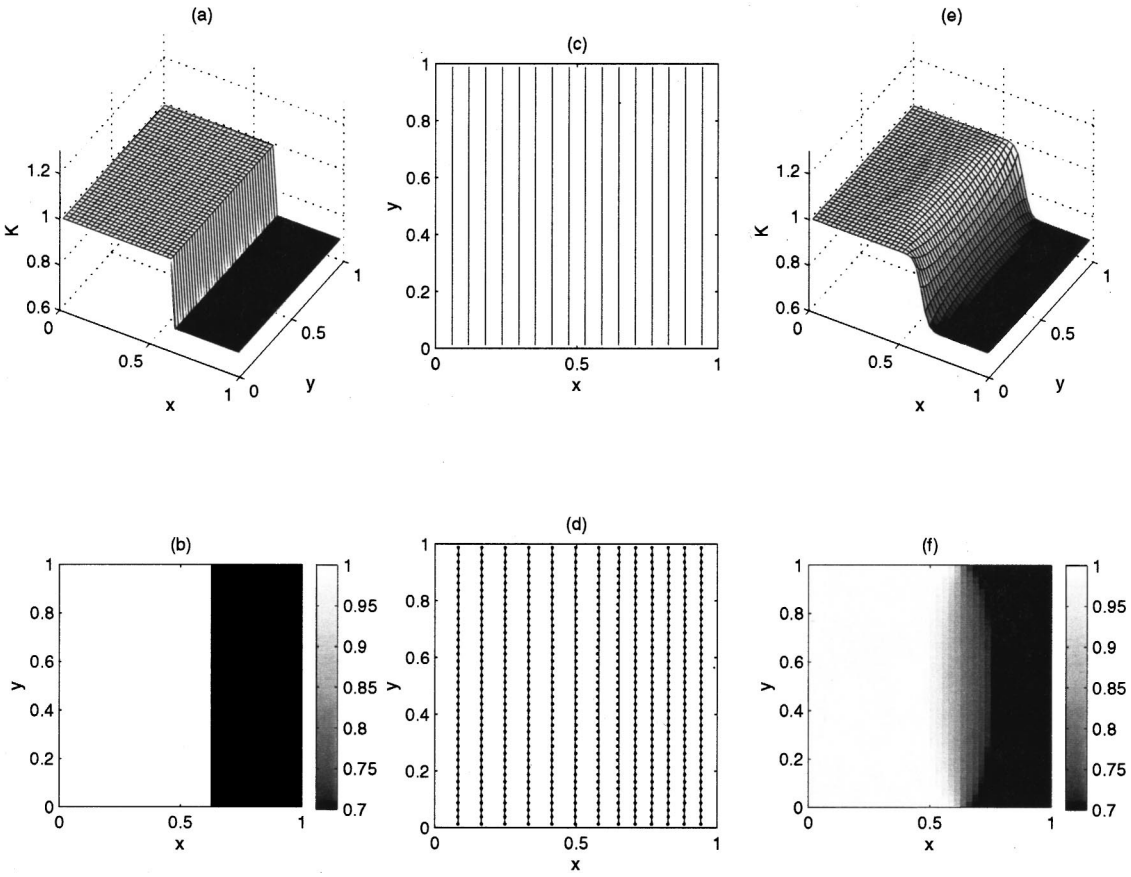

FIG. 1. Application of the direct inversion method to a layered system: (a) and (b) actual permeability plots; (c) actual arrival times; (d) actual (solid lines) and inverted (dotted lines) potential profiles; (e) and (f) inverted permeability plots.

motion) statistics. Each figure shows true and directly inverted permeability fields, along with true and directly inverted and potential profiles. In all these examples, the direct inversion was found to give very good results.

Figure 1 shows that the method handles well permeability contrasts transversely to the direction of displacement, with some expected dispersion around the discontinuity. Potential profiles are also reproduced well, again with some differences noted around the discontinuity. We must emphasize that, particularly in this example, the success of the method rests on the availability of the potential profile at the boundary, which removes the nonuniqueness of the problem. [Indeed for a 1D displacement at constant injection rate in a piecewise constant permeability, Eq. (10) becomes indeterminate.] Likewise, good results were found when the permeability contrast was in the direction parallel to the displacement. The ability of the method to invert the permeability field in the presence of an arbitrary closed region of sharp permeability contrast is discussed later.

The permeability field of Fig. 2 is smoothly varying and contains two peaks and one valley, with a permeability contrast of about 2. It was generated in a 64×64 grid using Franke's test function from MATLAB [12]. This function often serves as a test for the interpolation of scattered data. We first note that the arrival times are more sensitive to the heterogeneity than the pressure profiles, which are essentially parallel to the transverse direction. This feature was also noted in all other cases, where the permeability variation is relatively smooth. Figure 2 shows that the comparison between actual and inverted fields (in permeability and potential profiles) is very good. This example is characteristic of the success of the method in smoothly varying permeability fields.

A more stringent test is shown in Fig. 3 involving a similar permeability contrast. The permeability field is of the FBM type with a Hurst exponent $H=0.8$, and it is a typical example of a self-affine field, containing large-scale correlations [13]. FBM statistics with a Hurst exponent larger than 0.5 are often taken to describe the heterogeneity in the horizontal permeability of natural rocks [14]. Figure 3 shows that the match between actual and inverted data is also quite good. Potential profiles are closely matched. The inverted permeability reproduces well the main features of this field, specifically the regions where the permeability is high, medium, or low. However, discrepancies do exist in the detailed point-by-point variation of the permeability, the inverted field being somewhat smoother than the actual. The ability to capture long-wavelength, as opposed to high-frequency, variations is typical of this technique and was noted in other examples, as well. Figure 4 shows a statistical analysis of actual and inverted permeabilities. Histograms and the correlation structure (the semivariograms) match quite well, and the scatter plot is satisfactory. The dispersion around the 45° line indicates a small degree of point-by-point mismatch, as also evidenced in Fig. 3.

The direct inversion technique can be equally well applied to 3D geometries. Before we proceed, however, it is instructive to compare inversion results using the 2D stream-

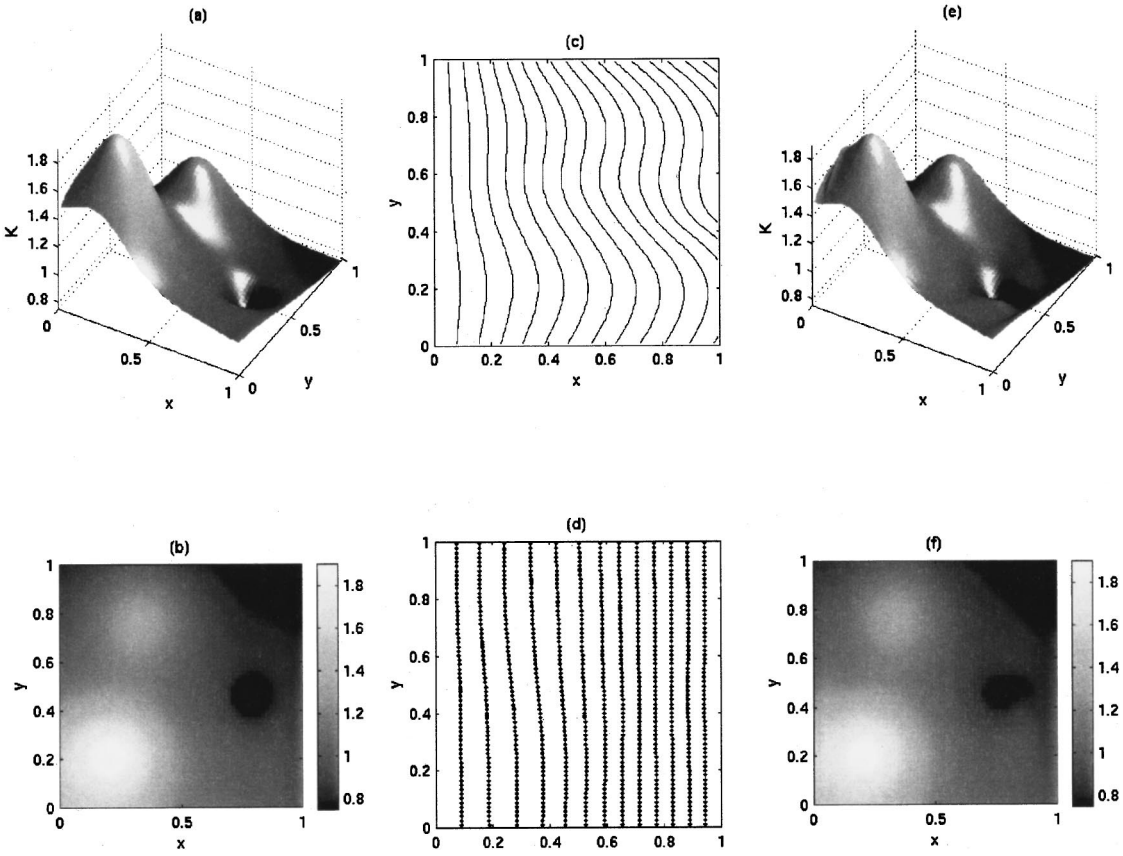

FIG. 2. Application of the direct inversion method to a smoothly varying field: (a) and (b) actual permeability plots; (c) actual arrival times; (d) actual (solid lines) and inverted (dotted lines) potential profiles; (e) and (f) inverted permeability plots.

function method described in the previous section. Figures 5 and 6 show the resulting permeability estimates, along with the associated stream functions, corresponding to Figs. 2 and 3, respectively. The streamlines are well reproduced, and the inverted permeability fields maintain the large correlation features. However, it is evident that the inverted fields miss many details. There are also apparent defects extending along slice-shaped regions, which arise from the integration along the arrival time contours. A statistical analysis, not shown here for lack of space, shows that the inverted permeability reproduces reasonably well the semivariograms. However, the histograms, and to a greater degree, the scatter plot, have large errors in several places. The stream-function method is prone to relatively large numerical errors, as it involves a threefold interpolation for spatial derivative estimation and the integration of hyperbolic equations (for determining the stream function). These weaknesses make the method unfavorable compared to the direct solution of Eqs. (9) and (10) (as seen in the comparison of Figs. 2–5 and 3–6). Advantages of the method, on the other hand, are that the permeability is inverted fast, compared to the previous, while one also readily obtains stream function and streamline profiles. These may be useful in certain applications, particularly in the field.

To demonstrate the applicability of the direct inversion method to three dimensions, we considered the 3D permeability field shown in Figs. 7(a) and 7(b), consisting of a log-normal distribution generated by the sequential Gaussian simulation, with a natural logarithmic mean of 2.0, a standard deviation of 0.2 and a dimensionless correlation length (with respect to the sample size) of 0.5. The permeability variation is somewhat larger than before. Characteristic arrival time contours from the simulation of the forward problem in a $16\times16\times16$ lattice are shown in Figs. 7(c) and 7(d). The direct inversion algorithm was applied by using a 3D version of Eq. (16) along with boundary conditions supplied from the forward problem. The results of the permeability inversion are shown in Fig. 8. They appear to be in relatively good agreement with the actual [Figs. 7(a) and 7(b)]. A more quantitative comparison is shown in the statistics of Fig. 9, calculated by GSLIB [15]. In general, the comparison is good. The inverted field shows a smaller range of variation than the actual, as reflected in both the semivariogram and the histogram. We note that the spatial correlation structure of the former is well captured in the inverted data. The scatter plot indicates a somewhat larger dispersion, compared to the FBM field of Figs. 3,4, which is expected, given the larger permeability contrast here.

In the above examples, where the permeability contrast is not too large, or where the permeability has relatively large spatial correlations, the direct inversion method gives good results. When the contrast increases and variations in permeability are sharper, however, the method is subject to increased errors. These arise primarily from the approximation of the spatial gradients of the arrival time in regions where the latter varies sharply. Figure 10 shows arrival time contours, calculated analytically (see the Appendix), for flow around an embedded circle of lower permeability. Even though the permeability contrast is relatively modest (0.6:1),

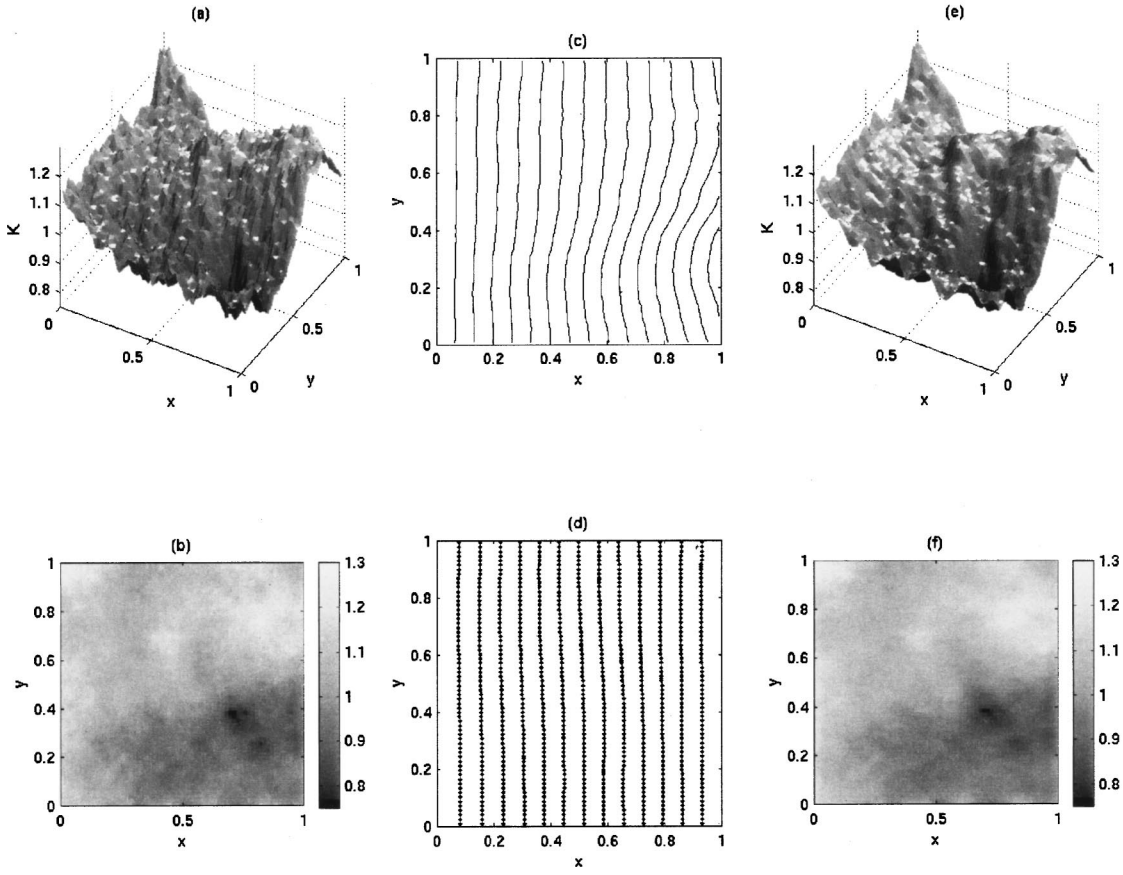

FIG. 3. Application of the direct inverse method to an FBM field with $H=0.8$: (a) and (b) actual permeability plots; (c) actual arrival times; (d) actual (solid lines) and inverted (dotted lines) potential profiles; (e) and (f) inverted permeability plots.

there exist two thin layers, extending downstream of the circle and centered around the two limiting streamlines tangent to the circle, where the arrival times exhibit sharp spatial variations. In these regions, the evaluation of the coefficients of Eq. (10) is likely to introduce errors and accordingly poor estimates for the permeability in certain places. These limiting streamlines also exist in any other fields containing regions of sharp permeability contrast. Because the respective layers extend downstream of the region of the sharp contrast, however, the associated errors in permeability estimates are different depending on the direction of displacement. We have conjectured, therefore, that the estimates of the direct method could be improved substantially, if we were to combine information from two different displacements, one in the forward and the other in the reverse direction.

IV. A HYBRID ALGORITHM

To circumvent the problems posed by high permeability contrasts we implemented the following hybrid procedure.

(1) Carry out a tracer displacement in the forward direction and directly invert to obtain one permeability estimate $k_f(\mathbf{x})$.

(2) Carry out a tracer displacement in the reverse direction and directly invert to obtain a second permeability estimate $k_b(\mathbf{x})$.

(3) Retain the estimates in those places, where they differ in absolute value by no more than a prescribed value, and discard in all others. Assign estimates in these regions by an interpolation algorithm (known in the geostatistics literature as kriging).

(4) Use an optimization algorithm (to be briefly described below) to fine-tune the so obtained composite permeability estimates.

The optimization algorithm is based on standard gradient methods [16] and will not be discussed here in detail. We briefly note that we used the following objective function:

$$\mathcal{J}=\frac{1}{2}\{[\mathbf{f}(\mathbf{k})-\mathbf{f}^m]^T\cdot\mathbf{W}_1\cdot[\mathbf{f}(\mathbf{k})-\mathbf{f}^m]+[\mathbf{k}-\mathbf{k}^p]^T\cdot\mathbf{W}_2\cdot[\mathbf{k}-\mathbf{k}^p]+[\mathbf{\Phi}_b-\mathbf{\Phi}_b^m]^T\cdot\mathbf{W}_s\cdot[\mathbf{\Phi}_b-\mathbf{\Phi}_b^m]\} \tag{17}$$

consisting of three inner product terms. The first is the weighted sum of the squares of the differences between the current estimates of the front arrival times $\mathbf{f}$ obtained from the simulator response, and the ''error-free'' data $\mathbf{f}^m$. The weight $\mathbf{W}_1$ is a diagonal matrix whose elements are the inverse of the variances of the errors of the measured arrival times. The third term is the analogous inner product for the differences between the current estimates for the potential at the no-flow boundaries $\mathbf{\Phi}_b$ and the data $\mathbf{\Phi}_b^m$, with $\mathbf{W}_3$ being the corresponding diagonal matrix. The second term represents the mismatch between the current permeability estimate $\mathbf{k}$ and its prior $\mathbf{k}^p$. It is a regularization term, as required by Tikhonov's theory [17], and restricts the parameters being optimized to not deviate greatly from the

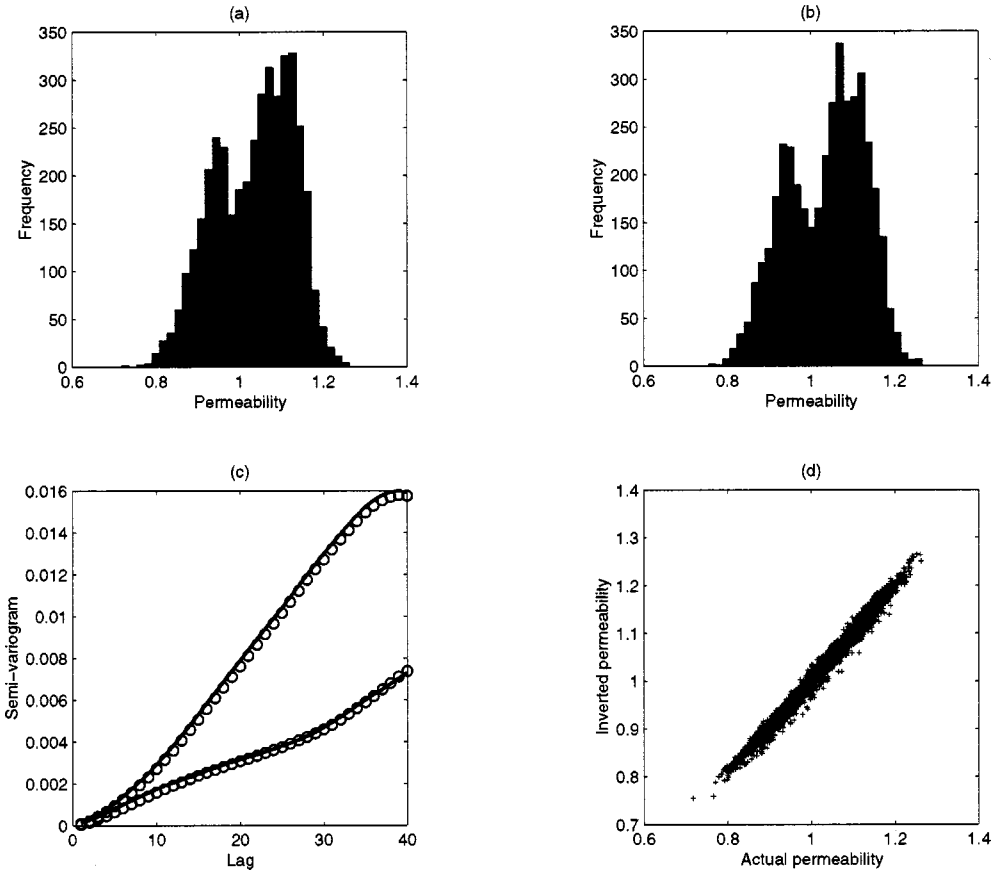

FIG. 4. Statistical comparison between actual and inverted permeabilities of Fig. 3: (a) histogram of actual permeability; (b) histogram of inverted permeability; (c) semivariogram in two different directions of the actual (solid lines) and inverted (circles) data; (d) scatter plot of actual and inverted data.

prior information. Here, $\mathbf{W}_2$ denotes the inverse of the covariance matrix of the prior. Numerical experience has demonstrated its necessity for stable and convergent solutions. However, the accuracy of the initial guess plays a pivotal role in the convergence to the true solution. It is in this context that the hybrid algorithm offers an important advantage. In our method, the prior information is supplied using the direct inversion method, outlined in steps 1–3 above, which is generally close to the true permeability field. As a result, in many of the cases tried, the optimization method converges close to the true values. By contrast, in other related inverse problems, the prior permeability is typically generated by a geostatistical algorithm constrained to (usually) sparse measurements, and its convergence to the true solution is generally uncertain (e.g., see Ref. [18]). At the same time, we must stress that we have also encountered

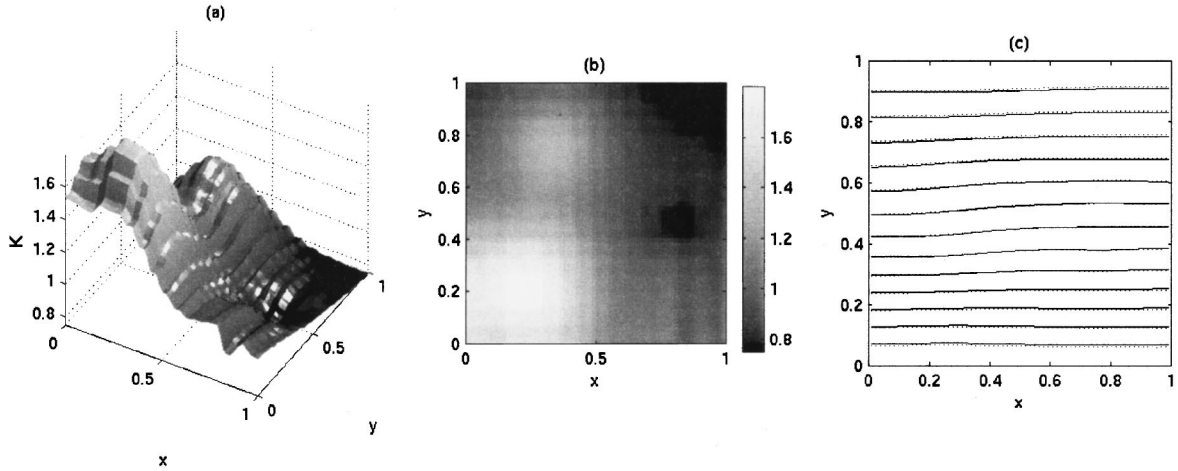

FIG. 5. Application of the stream-function approach to the medium of Fig. 2: (a) and (b) inverted permeability plots; (c) actual (solid lines) and inverted (dotted lines) streamlines.

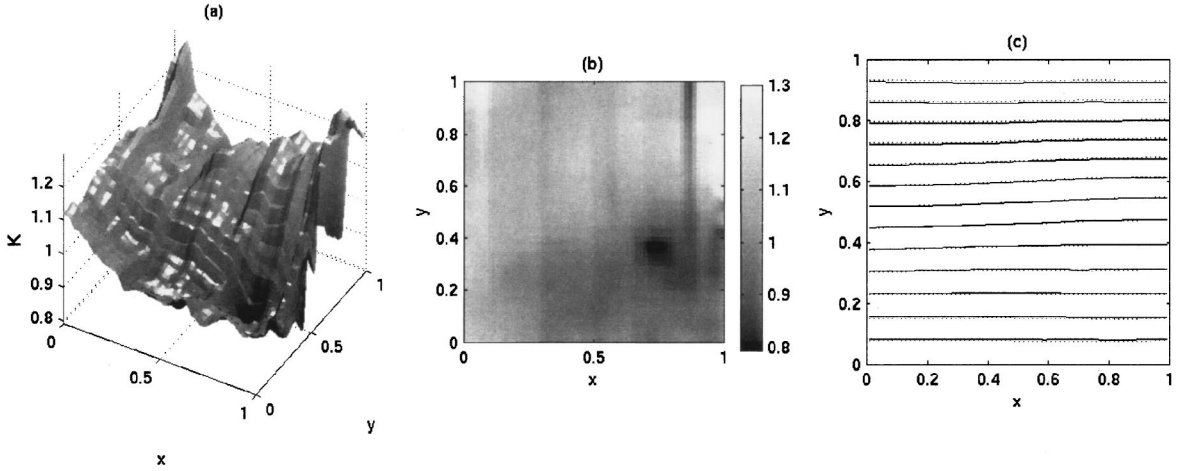

FIG. 6. Application of the stream-function approach to the medium of Fig. 3: (a) and (b) inverted permeability plots; (c) actual (solid lines) and inverted (dotted lines) streamlines.

many problems involving sharp permeability contrasts, which cannot be successfully handled even with the hybrid algorithm, as shown below. For completeness, we mention that in order to match arrival times and boundary pressures as well as possible, we often had to increase their weights in the objective function by multiplying with a large number.

Applications of the hybrid algorithm using simulated data are illustrated in Figs. 11–14 for three different examples. The medium in Fig. 11 contains two blocks of low permeability with a 1:5 contrast. This particular configuration corresponds to the experimental Hele-Shaw cell used in Ref. [19], and was discretized by a 22×10 lattice. The top of Fig. 11 [panels (a), (b)] shows the prior estimate fed to the optimization algorithm, following steps 1–3. Due to the sharp permeability contrast between low and high permeable regions, the spatial derivatives of the arrival times have significant numerical errors in certain regions, and lead after steps 1 and 2 to a mismatch between true and inverted values in

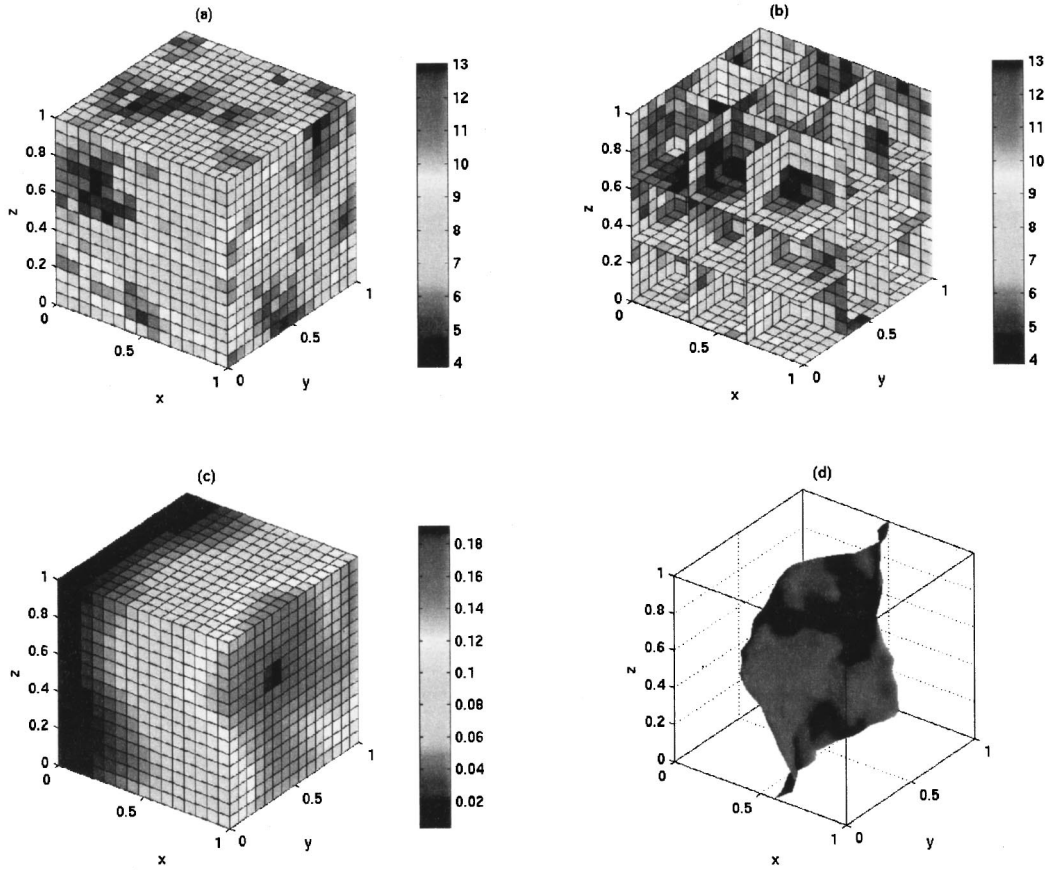

FIG. 7. A 3D permeability field and corresponding arrival times: (a) and (b) the actual permeability field in different cross-sections; (c) the arrival time distribution; (d) arrival time isosurface at $t=0.07$.

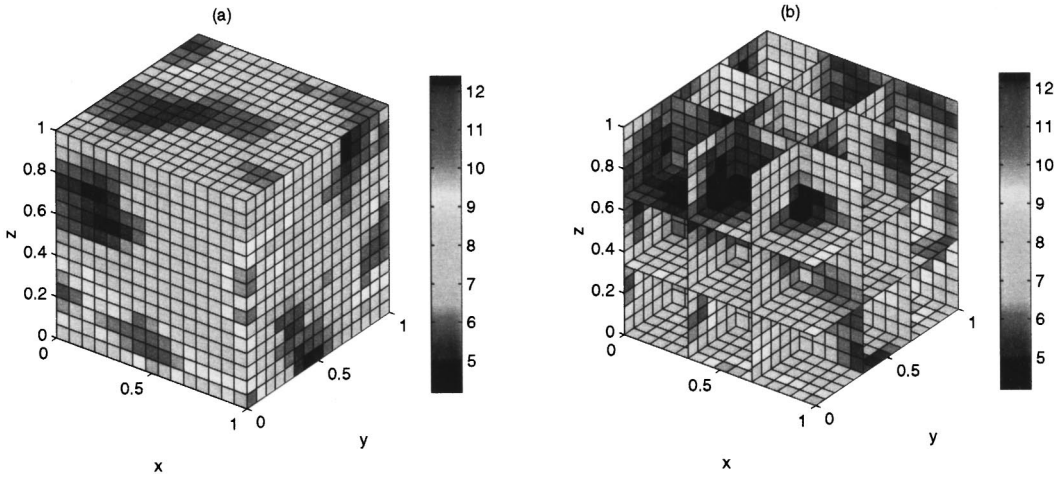

FIG. 8. Application of the direct inversion method to the 3D field of Fig. 7: (a) and (b) representation of the inverted data in different cross sections.

various places. Through step 3 (where estimates were discarded when they differed by more than 30%), these errors have been minimized. The directly inverted field, after step 3 [Figs. 11(a), 11(b)] has the main trends of the true field, although it is obvious that the contrast is not as sharp as the actual, and is in need of fine-tuning. Results following the application of the optimization algorithm of step 4, using 40 iterations, and based on the initial guess after kriging [Figs. 11(a), 11(b)], is shown in the middle of Fig. 11 [panels (c), (d)]. The results are much improved and, with a few exceptions, they are very close to the actual. Although not shown, potential and arrival time profiles are also matched very well. By contrast, if in the optimization algorithm we used a uniform initial guess, instead of that corresponding to the direct method [panels (a), (b) in Fig. 11], the resulting estimate (after the same number of iterations) is poor in many places,

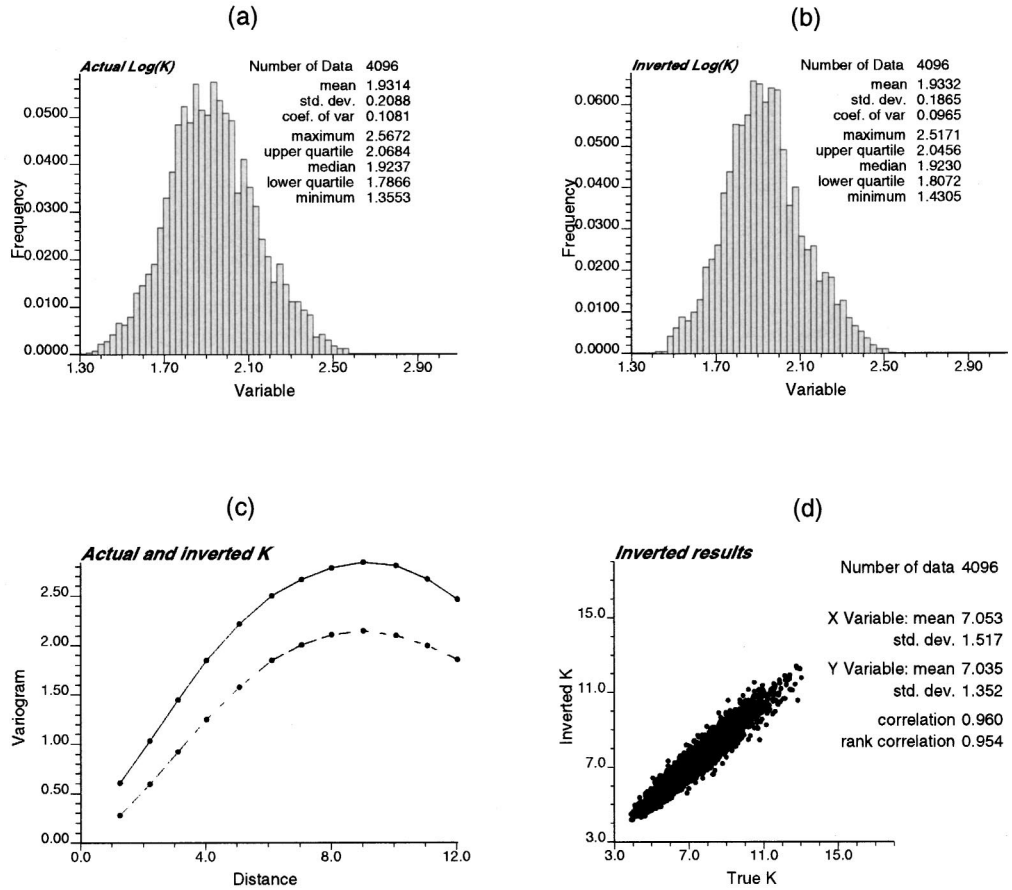

FIG. 9. Statistical comparison between actual and inverted permeabilities of Fig. 8: (a) histogram of actual permeability; (b) histogram of inverted permeability; (c) omnidirection semivariogram of the actual (solid lines) and inverted (dash lines) data; (d) scatter plot of actual and inverted data.

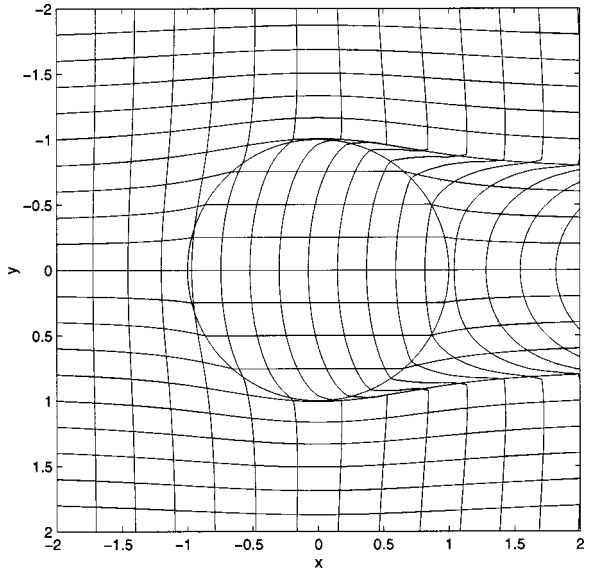

FIG. 10. Streamlines and arrival time contours corresponding to a medium of uniform permeability in which a circular inclusion of lower permeability is embedded (permeability contrast is 0.6:1). The contours are calculated analytically (see Appendix). Displacement is from left to right.

as shown in the bottom of Fig. 11 [panels (e), (f)]. This is despite the fact that arrival times and potential profiles are also matched very well. We conclude that, at least for this example, the application of the hybrid method gives a substantial improvement.

Figure 12 shows the application of the algorithm to a correlated log-normal distribution with a logarithmic mean of 2.0, a standard deviation of 0.5 and a dimensionless correlation length of 0.25. In this example, the block-to-block permeability variation is much larger than in the FBM field of Fig. 3 or the 3D field of Fig. 7, the largest contrast being of an order of magnitude. The application of the direct inversion method followed by kriging leads to the results shown in the middle of Figs. 12(c), 12(d). Although capturing the general features of the true field, the estimates are generally coarser and smoother than the actual values. Comparison of arrival times and potential profiles based on the inverted field (not shown for lack of space) indicates a mismatch with the actual in certain places. To fine-tune the results and recover some of the high-frequency variations, we applied the optimization algorithm of step 4. Results after 40 iterations are shown on the right of Figs. 12(e), 12(f). The algorithm does not fully reproduce the actual field, and some

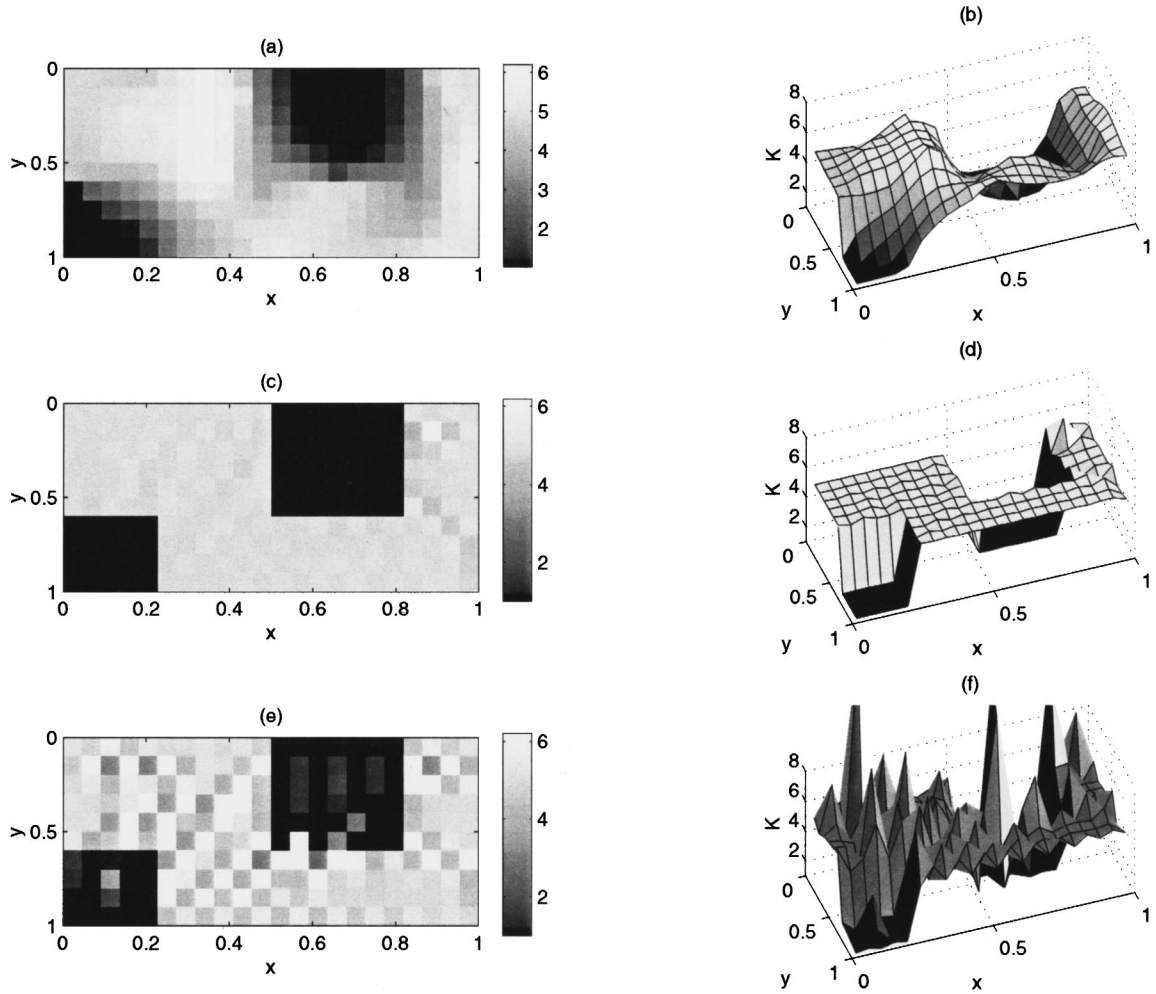

FIG. 11. Application of the hybrid algorithm to a system with block discontinuities in permeability (permeability contrast is 1:5): Top two plots (a) and (b) show permeability estimates after steps 1–3 (kriging). Middle two plots (c) and (d) show permeability estimates after step 4 (optimization). Note the closeness to the actual data. Bottom two plots (e) and (f) show permeability estimates using the optimization method but with a uniform permeability initial guess.

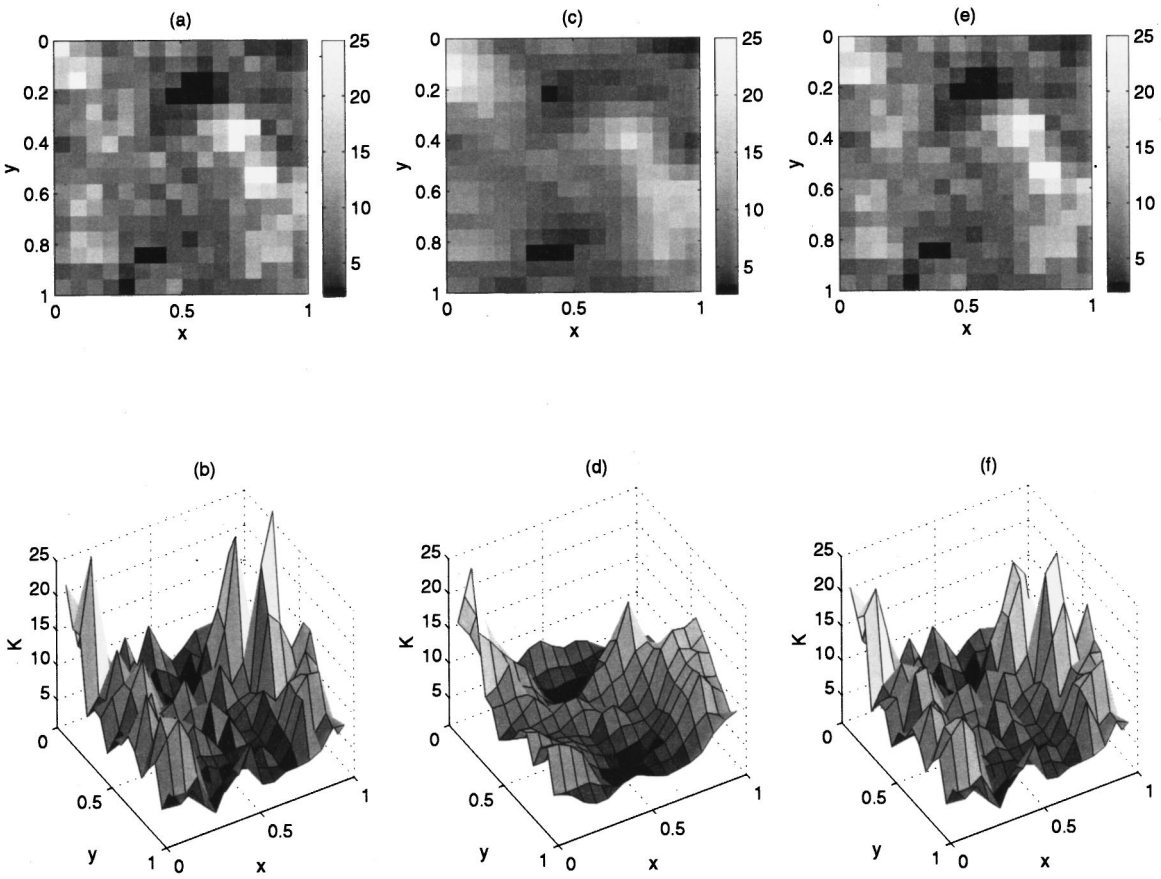

FIG. 12. Application of the hybrid algorithm to a field with a log-normal distribution with maximum contrast of about 10: (a) and (b) actual permeability plots; (c) and (d) plots of permeability estimates after steps 1–3 (kriging); (e) and (f) plots of permeability estimates after step 4 (optimization). Note that the cutoff value of the colorbars in the image plots is set at 25.

errors around large variations of permeability are detectable. However, it is obvious that a significant improvement has been achieved. Figure 13 shows the corresponding statistical comparison. The mean and the variance from the hybrid algorithm agree very well with the actual. (By contrast, in results that are not shown here, the variance from kriging is underestimated by about 20%, although the mean is the same.) The two histograms are roughly equal, while the semivariograms have the same correlation structure. The scatter plot shows that good agreement exists over a good range of lower permeabilities, although an increasing scatter can be seen at larger permeabilities. In this example, these are typically associated with large contrasts. We need to reiterate that the success of the hybrid algorithm depends to a large extent on the accuracy of the initial guess, which is here provided by the direct method and positions the optimization scheme close to the true solution. By contrast, the estimates resulting from the application of the same optimization algorithm after bypassing steps 1–3 and utilizing a uniform initial guess were quite poor, even though arrival times and potential matched nearly perfectly with the true values.

At the same time, we must point out that we have also encountered several cases where the hybrid algorithm was not as successful as desired. Figures 14(a), 14(b) are examples of a ''checkerboard-pattern'' heterogeneous field, with a permeability contrast of 1:4. A pattern similar to this was used in some previously reported tracer displacement experiments [20]. The results of the algorithm at the end of the kriging step are shown in the middle of Figs. 14(c), 14(d). The mismatch with the true data is quite apparent. The 2D projection in the middle of Fig. 14 reproduces roughly the places of maximum permeability variation, but the picture is clearly ''out of focus.'' The results of the application of the optimization method are shown in the right of Figs. 14(e) and 14(f). We note a clear improvement, compared to the previous step, and a better focused image. Yet, there is also clear evidence of mismatches in various places, including a smoothing of the sharp contrast around the edges of discontinuity, and of other defects, which altogether preclude an exact matching. Thus, although overall the hybrid algorithm appears to be a promising alternative in cases involving large contrasts, we caution that this is not uniformly true and that many counterexamples can readily be constructed where this algorithm will not be as successful.

Sensitivity study. The sensitivity of the algorithm to sharp permeability contrasts is a reflection of its relatively weak robustness to errors in arrival time and/or boundary pressure. To asses the latter, we studied the sensitivity of the directly inverted permeability values to random errors in the arrival time and the boundary pressure, using again synthetic data. For this purpose, the forward numerical solutions for the arrival time and boundary pressure, $\mathbf{f}^m$ and $\mathbf{\Phi}_b{}^m$, respectively, assumed to represent true (error-free) results, were randomly perturbed as follows

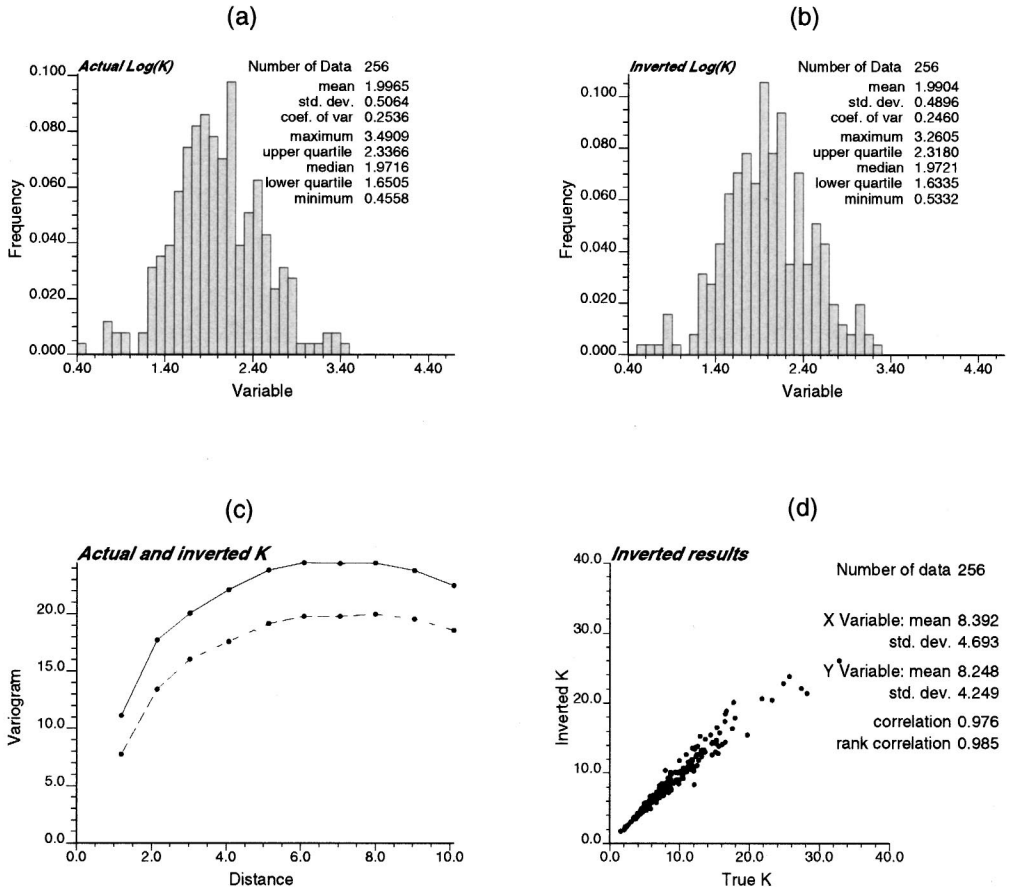

FIG. 13. Statistical comparison between actual and inverted (after steps 1–4) permeabilities of Fig. 12: (a) histogram of actual permeability; (b) histogram of inverted permeability; (c) omnidirection semivariogram of the actual (solid lines) and inverted (dash lines) data; (d) scatter plot of actual and inverted data.

$$\mathbf{f}_\epsilon = \mathbf{f}^m + \theta_\epsilon \min[\mathbf{f}^m] \tag{18}$$

and

$$\mathbf{\Phi}_{b_\epsilon} = \mathbf{\Phi}_b{}^m + \theta_\epsilon \min[\mathbf{\Phi}_b{}^m], \tag{19}$$

where θ_ϵ is a random Gaussian noise with mean equal to zero and standard deviation equal to ϵ. The minimum taken in Eqs. (18) and (19) reflects the assumption that in a realistic experiment, the resolution of the measuring device is independent of the value of the quantity being measured. The results from Eqs. (18) and (19) were then used in Eqs. (9) and (10) to invert the permeability field following the hybrid algorithm.

Shown in Fig. 15 are the sensitivity results for the permeability field of Fig. 12 (inversion error vs ϵ). Two curves are shown, one corresponding to the full hybrid algorithm (steps 1–4) and another corresponding to the results after only steps 1–3 were completed, namely, after kriging the direct estimates from the forward and backward displacements. As a measure of the inversion error, we used the standard deviation of the inverted from the true permeability, normalized with respect to the mean, the error in the input data being proportional to ϵ. For each ϵ, a total of ten realizations were performed. The curves in Fig. 15 represent the mean values of the results obtained, with the standard deviation also denoted. First, we observe that even in the case of ''error-free'' input, the inverted data have a residual error. This was already noted in the discussion of Fig. 12, and was attributed to the relatively sharp changes in permeability for that field. We also note that inversion errors, following the full hybrid algorithm, are considerably smaller than those based on kriging, as also discussed before. As the error in the input data increases, however, the inversion errors for the hybrid algorithm, both in mean and variance, increase faster than those based on kriging. In fact, the latter is actually not very sensitive to errors in the input data, and in a sense is quite robust compared to the full hybrid algorithm. The latter outperforms kriging at small values of input error. However, it is subject to increasing inversion errors beyond a certain level of input error. The origin of this discrepancy is due to the two different objectives satisfied by the two algorithms. In the hybrid algorithm, the optimization aims to match arrival time and pressure data (even if they are inaccurate). In kriging, this matching is ignored, after the completion of steps 1 and 2. Similar behavior was found with other types of synthetic permeability fields used. We conclude that the successful implementation of the technique proposed relies on input data of good accuracy.

V. DIRECT INVERSION ALGORITHM: ANISOTROPIC MEDIA

On the other hand, a strong attribute of this technique is that it can be applied to anisotropic porous media. In this

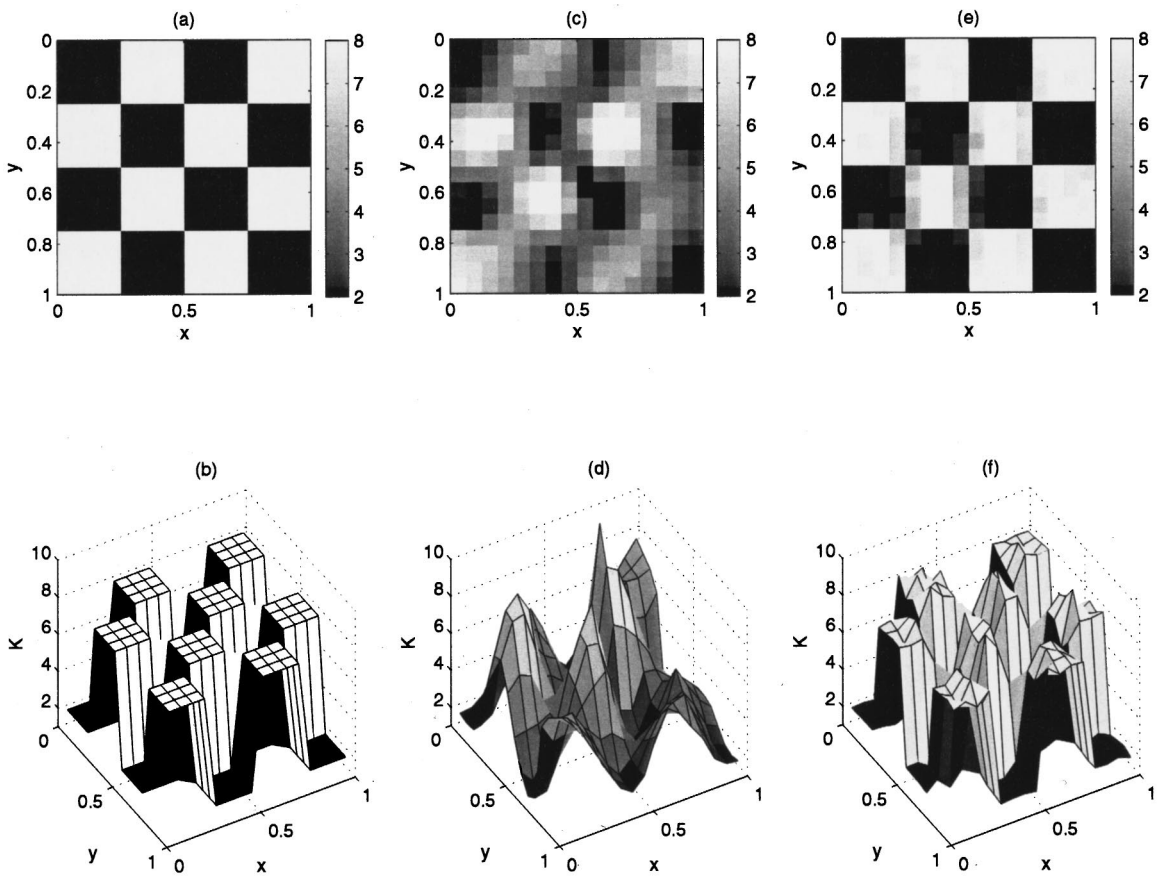

FIG. 14. Application of the hybrid algorithm to a checkerboard permeability pattern (contrast is 2:8): (a) and (b) actual permeability plots; (c) and (d) plots of permeability estimates after steps 1–3 (kriging); (e) and (f) plots of permeability estimates after step 4 (optimization). Note that the cutoff value of the colorbars in the image plots is set at 8.

section, we consider for simplicity 2D geometries, where the principal directions of the permeability tensor are constant and coincide with the rectangular coordinates x and y, namely, we take

$$\mathbf{K}=\begin{vmatrix} k_x(\mathbf{x}) & 0 \\ 0 & k_y(\mathbf{x}) \end{vmatrix}. \tag{20}$$

An extension to the more general case is under consideration and will be presented elsewhere. Under these conditions, the equations analogous to Eqs. (9) and (10) read

$$(\mathbf{K}\cdot\nabla\Phi)\cdot\nabla f=-\phi(\mathbf{x}) \tag{21}$$

and

$$\nabla(\cdot\,\mathbf{K}\cdot\nabla\Phi)=0. \tag{22}$$

Using scalar notation, and substituting from Eq. (20), we further have

$$k_x\frac{\partial\Phi}{\partial x}\frac{\partial f}{\partial x}+k_y\frac{\partial\Phi}{\partial y}\frac{\partial f}{\partial y}=-\phi \tag{23}$$

and

$$\frac{\partial}{\partial x}\left[k_x\frac{\partial\Phi}{\partial x}\right]+\frac{\partial}{\partial y}\left[k_y\frac{\partial\Phi}{\partial y}\right]=0. \tag{24}$$

Equations (23) and (24) constitute a pair of two equations in three unknowns (k_x, k_y, and Φ) and require additional information for their solution. One possible approach, by which this information can be obtained, is by conducting two

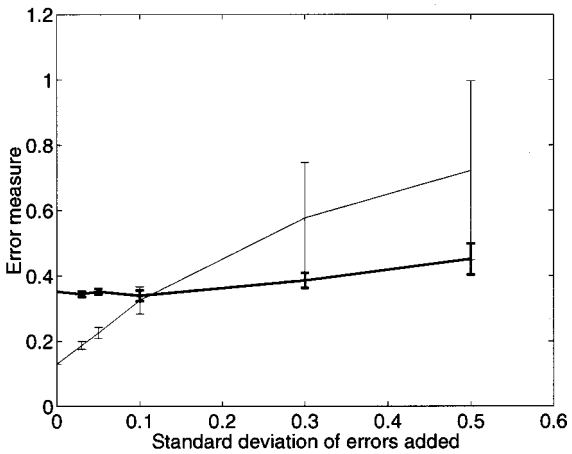

FIG. 15. Sensitivity of the inverted permeability field of Fig. 12 to errors in arrival times and boundary pressure data. Inversion based on the hybrid algorithm (steps 1–4) (thin line) and on the kriging algorithm (steps 1–3) (thick line). The error measure is the normalized standard deviation of the inverted from the actual permeabilities. The input error is as described in Eqs. (18) and (19).

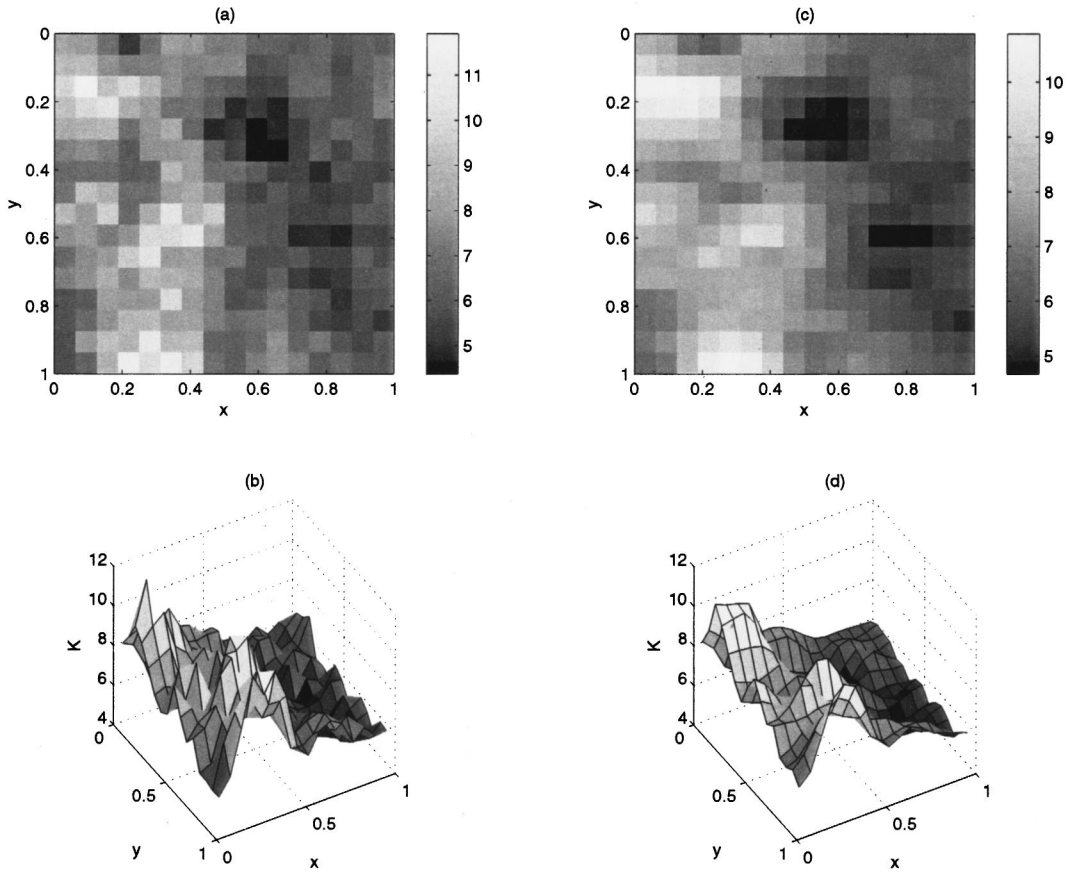

FIG. 16. Application of the direct inversion method to an anisotropic field with known and fixed principal axes of anisotropy. Results for k_x: (a) and (b) plots of the actual permeability component values; (c) and (d) plots of the inverted permeability component values.

tracer displacements, one in the x direction with no-flow boundaries perpendicular to the y axis, and another in the y direction with no-flow boundaries perpendicular to the x axis. If we denote the arrival time functions and the potentials of the two displacements by f_{I} and f_{II}, and Φ_{I} and Φ_{II}, respectively, Eq. (23) becomes

$$k_x \frac{\partial \Phi_{\mathrm{I}}}{\partial x}\frac{\partial f_{\mathrm{I}}}{\partial x} + k_y \frac{\partial \Phi_{\mathrm{I}}}{\partial y}\frac{\partial f_{\mathrm{I}}}{\partial y} = -\phi, \tag{25}$$

$$k_x \frac{\partial \Phi_{\mathrm{II}}}{\partial x}\frac{\partial f_{\mathrm{II}}}{\partial x} + k_y \frac{\partial \Phi_{\mathrm{II}}}{\partial y}\frac{\partial f_{\mathrm{II}}}{\partial y} = -\phi \tag{26}$$

for the respective displacements. Then, the permeability components can be determined from the two equations

$$k_x = -\frac{\phi}{A}\left[\frac{\partial \Phi_{\mathrm{II}}}{\partial y}\frac{\partial f_{\mathrm{II}}}{\partial y} - \frac{\partial \Phi_{\mathrm{I}}}{\partial y}\frac{\partial f_{\mathrm{I}}}{\partial y}\right] \tag{27}$$

and

$$k_y = -\frac{\phi}{A}\left[\frac{\partial \Phi_{\mathrm{I}}}{\partial x}\frac{\partial f_{\mathrm{I}}}{\partial x} - \frac{\partial \Phi_{\mathrm{II}}}{\partial x}\frac{\partial f_{\mathrm{II}}}{\partial x}\right], \tag{28}$$

where

$$A = \frac{\partial \Phi_{\mathrm{I}}}{\partial x}\frac{\partial f_{\mathrm{I}}}{\partial x}\frac{\partial \Phi_{\mathrm{II}}}{\partial y}\frac{\partial f_{\mathrm{II}}}{\partial y} - \frac{\partial \Phi_{\mathrm{II}}}{\partial x}\frac{\partial f_{\mathrm{II}}}{\partial x}\frac{\partial \Phi_{\mathrm{I}}}{\partial y}\frac{\partial f_{\mathrm{II}}}{\partial y} \tag{29}$$

given the data f_{I} and f_{II}, and the calculated potentials Φ_{I} and Φ_{II}. The latter can be obtained by solving Eq. (24), with k_x and k_y given by Eqs. (27)–(29), and with the appropriate boundary conditions corresponding to the two different displacements. The following iterative algorithm was implemented to solve the resulting coupled system.

(1) Based on the v-level estimates for the potentials Φ_{I}^{ν} and Φ_{II}^{ν}, use Eqs. (27) and (28) to estimate the v-level iterates k_x^{ν} and k_y^{ν}. At the initial level ($\nu=0$), an initial guess, typically in the form of a linear variation, was supplied for the potentials.

(2) Based on explicit (v-level) estimates for k_x^{ν} and k_y^{ν}, integrate Eq. (24) twice, using SOR finite differences to calculate the potentials at the next iteration level, $\Phi_{\mathrm{I}}^{\nu+1}$ and $\Phi_{\mathrm{II}}^{\nu+1}$.

This algorithm was found to work well for the various cases tested.

The method was subsequently applied to the anisotropic permeability field shown in the left of Figs. 16 and 17 [panels (a), (b)]. Its statistics are similar to Fig. 7, and involve a log-normal spatially correlated distribution with the same mean and standard deviation. By simulating a forward tracer displacement in the two directions, x and y, respectively, we obtained arrival time functions and potentials at the no-flow boundaries, which were then used for the inversion according to the above scheme. The directly inverted fields (in the absence of optimization or kriging) are shown in the right of the two Figs. 16 and 17 [panels (c), (d)]. Given the coupled

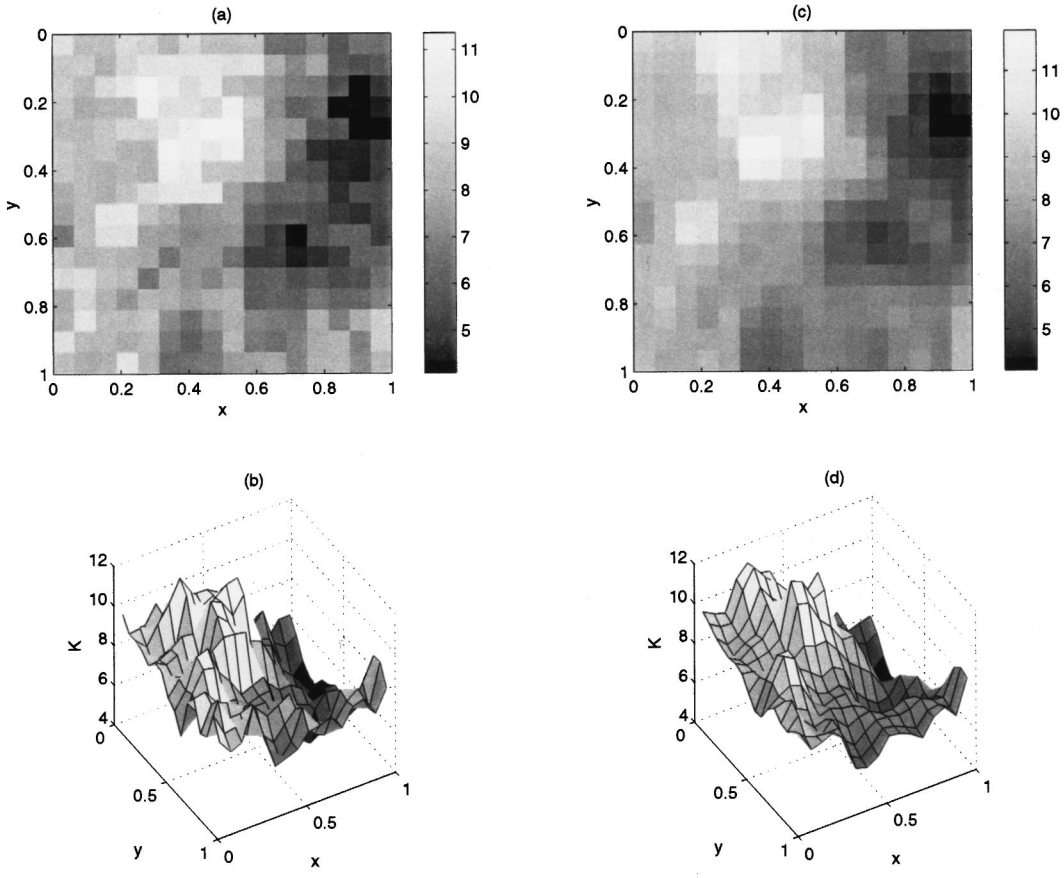

FIG. 17. Application of the direct inversion method to an anisotropic field with known and fixed principal axes of anisotropy. Results for k_y: (a) and (b) plots of the actual permeability component values; (c) and (d) plots of the inverted permeability component values.

nature of the problem, the reconstruction of the two permeability components can be considered generally good. The method reproduces relatively well the regions of high and low permeability. Compared to the isotropic case under the same permeability contrast, however, the reconstruction is not as sharp, and the projections of the inverted images appear slightly ''out of focus'' in certain places. This reflects an underlying mismatch in the arrival times and the potential profiles, which is not shown here. Further work is under way to improve the algorithm and fine-tune the direct inversion method, including the implementation of a hybrid algorithm, as in the isotropic case.

VI. CONCLUDING REMARKS

In this paper we presented a method for the direct inversion of the permeability of porous media, based on arrival time contours and information on the pressure profiles at the boundaries. In real systems, the former can be obtained using techniques of visualization, computerized tomography (or seismic and cross-hole tomography for field applications). The method utilizes Darcy's law for flow in porous media in combination with the kinematics of flow, as expressed in the arrival times, to derive a boundary-value problem, the solution of which leads to a direct reconstruction of the permeability field. An important feature of the technique is that it requires information from the pressure at the boundaries, to solve an ellipticlike formulation, rather than the two hyperbolic equations, which formally describe the problem. The algorithm developed is a rigorous, although not necessarily robust, tool for the analysis of arrival time contours.

Using simulated data, the method was found to work well for cases where the permeability contrast is not very large, and the field is spatially correlated. In general, the technique captures well variations corresponding to larger wavelengths, but not as well fine-scale details. For sharper contrasts, a hybrid version of the algorithm was developed, in which the direct method is used to generate the initial guess in an optimization algorithm. The hybrid version minimizes the sensitivity of the method to errors in spatial derivatives, which are augmented in the presence of sharp contrasts. Numerical examples in two and three dimensions using simulated (assumed ''error-free'') data demonstrated that the hybrid algorithm works well and that it is superior to the more conventional case, where the initial input is a uniform distribution. However, other examples can also be constructed, involving sharp contrasts and/or errors in the input data, where the inversion technique is not as satisfactory and requires further improvement. A sensitivity analysis showed that the method is prone to increasing inversion errors, as the quality of the input data deteriorates. On the other hand, a nontrivial advantage of the direct inversion technique is its potential to invert the permeability tensor in anisotropic porous media. Preliminary results for the case where the principal axes of anisotropy are fixed and known were presented and found to be promising. Further work is currently under way to fine-tune the method and to also extend it to the more general

case, where the permeability tensor is full.

The various requirements for its implementation suggest that the technique proposed is best suited for laboratory applications. Even then, its applicability relies on several conditions: the availability of pressure profiles at the system boundaries, the absence, or the minimization, of dispersion during the tracer displacement and the adequate resolution in arrival time contours. The first requirement appears to be the most difficult to meet, in view of the demand for adequate spatial resolution, which presently available tools may not possess, and the need to enforce Darcy's law near no-flow boundaries. Alternatively, this profile can be obtained by locally probing the surfaces with a minipermeameter to construct a surface permeability map, from which the pressure profile can be computed. A certain amount of pore-scale dispersion in real porous media is also unavoidable, given that the dispersion coefficient is proportional to the velocity, thus leading to a constant Peclet number and a finite amount of dispersion. However, for relatively small dispersivities, such dispersion effects could be minimal. Sufficient spatial resolution on arrival times would allow to capture fine-scale variations, at the expense of increased computational time in the optimization routine of the hybrid algorithm, and possible instabilities as the degree of resolution increases and the input error increases. However, it must also be remarked that in our experience, so far, a coarse-grid reconstruction can adequately capture the large-scale features of the permeability field, both in the isotropic and the anisotropic cases.

Regarding field applications, the absence of boundary pressure data and the difficulty in conducting displacements in different directions, impose constraints that make difficult the application of the present technique. One could still use arrival time contours, if available through seismic or crosshole tomography, to reconstruct streamfunctions and streamtubes, as outlined in the text for a 2D problem. However, such information is not sufficient for the inversion of the permeability field, although it may be useful for other purposes.

ACKNOWLEDGMENTS

This research was partly supported by DOE Contracts No. DE-FG22-96BC1994/SUB and DE-AC26-99BC15211, the contributions of which are gratefully acknowledged. We would like to thank Roland Lenormand and Dominique Salin for useful comments and discussions. The contribution of the NATO travel Grant No. CRG 973049 is also gratefully acknowledged.

APPENDIX: ARRIVAL TIMES FOR CIRCULAR PERMEABILITY HETEROGENEITY

In this appendix, we provide analytical solutions for a simple 2D problem involving tracer displacement in an infinite domain of constant permeability 1, in which a circular inclusion of radius $r=1$ and permeability κ is embedded. Hence, the permeability is the step function

$$k=(1-\kappa)H(r-1)+\kappa. \tag{A1}$$

To solve this problem, we subtract the homogeneous solution $(-x)$ from the potential, and thus consider the problem

$$\nabla\cdot[k\nabla(x-\psi)]=0, \tag{A2}$$

where $\psi=\Phi+x$. In view of Eq. (A1) this further reads

$$\nabla\cdot(k\nabla\psi)=-(1-\kappa)\,\delta(r-1)\,\frac{x}{r}, \tag{A3}$$

where δ denotes the Dirac delta function. To solve Eq. (A3) we use polar coordinates (r,θ) and the following interface conditions at the place of permeability discontinuity:

$$\psi|_{r=1_+}=\psi|_{r=1_-} \tag{A4}$$

and

$$\kappa\frac{\partial\psi}{\partial r}\bigg|_{1-}-\frac{\partial\psi}{\partial r}\bigg|_{1+}=(1-\kappa)\cos\theta. \tag{A5}$$

The solution follows readily

$$\psi=\left(\frac{1-\kappa}{1+\kappa}\right)r\cos\theta;\quad r\leqslant 1, \tag{A6}$$

$$\psi=\left(\frac{1-\kappa}{1+\kappa}\right)\frac{1}{r}\cos\theta;\quad r>1, \tag{A7}$$

from which the velocity components can be calculated. We find,

$$v_x=\frac{2\kappa}{1+\kappa};\quad r\leqslant 1,$$

$$v_x=1+\left(\frac{1-\kappa}{1+\kappa}\right)\frac{y^2-x^2}{(x^2+y^2)^2};\quad r>1,$$

and

$$v_y=0;\quad r\leqslant 1,$$

$$v_y=-\left(\frac{\kappa(1-\kappa)}{1+\kappa}\right)\frac{2xy}{(x^2+y^2)^2};\quad r>1.$$

Thus, the streamlines are the solution of

$$\frac{dy}{dx}=0;\quad r\leqslant 1,$$

$$\frac{dy}{dx}=-\frac{2(1-\kappa)xy}{(1+\kappa)(x^2+y^2)^2+(1-\kappa)(y^2-x^2)};\quad r>1,$$

from which the arrival times are obtained by integrating along the streamlines

$$t-t_0=\int_{x_0}^{x}\frac{\phi}{u_x(x',y)}\,dx', \tag{A8}$$

where ϕ is the porosity. These results were used to compute the streamlines and the arrival time contours of Fig. 10 in the text.

[1] L. W. Lake, *Enhanced Oil Recovery* (Prentice Hall, Englewood Cliffs, NJ, 1989); L. W. Gelhar, *Stochastic Subsurface Hydrology* (Prentice-Hall, Englewood Cliffs, NJ, 1993).

[2] W. G. Yeh, Water Resour. Res. **22**, 95 (1986); N. Z. Sun, *Inverse Problems in Groundwater Modeling* (Kluwer Academic, Netherlands, 1994); D. McLaughlin and L. R. Townley, Water Resour. Res. **32**, 1131 (1996).

[3] C. S. Matthews and D. G. Russell, *Pressure Buildup and Flow Tests in Wells* SPE Monograph Vol. 1 (SPE, Dallas, 1967); R. C. Earlougher, *Advances in Well Test Analysis*, SPE Monograph Vol. 5 (SPE, Dallas, 1977); R. N. Horne, *Modern Well Test Analysis* (Petroway, Palo Alto, CA, 1995).

[4] S. C. Jones in Proceedings of the Society of Petroleum Engineers 67th Annual Meeting, 1992 (SPE, 1992), paper no. 24757; S. Ganapathy, D. Wreath, G. Pope, and K. Sepehrnoori, Soc. Pet. Eng. Formation Evaluation **9**, 273 (1993).

[5] C. F. Harvey and S. M. Gorelick, Water Resour. Res. **31(7)**, 1615 (1995); B. J. Wagner, J. Hydrology **135**, 275 (1992); A. Datta-Gupta, S. Yoon, I. Barman, and D. W. Vasco, J. Pet. Technol. **50**, 72 (1998).

[6] D. C. Brock and F. M. Orr, in Proceedings of the Society of Petroleum Engineers 66th Annual Meeting, 1991 (SPE, 1991), paper no. 22614.

[7] E. M. Withjack, S. M. Graham, and C. T. Yang, Soc. Pet. Eng. Formation Evaluation **7**, 447 (1991).

[8] D. E. Lumley and R. A. Behrens, Soc. Pet. Eng. Res. Evaluation Eng. **1**, 528 (1998).

[9] L. Zhan and Y. C. Yortsos (unpublished).

[10] Z-M. Yang and Y. C. Yortsos, Phys. Fluids **9**, 286 (1997).

[11] J. A. Sethian, *Level Set Methods and Fast Marching Methods* (Cambridge University Press, New York, 1999).

[12] *Spline Toolbox User's Guide* (The Mathworks, Inc., 1999).

[13] R. F. Voss, in *The Science of Fractal Images* (Springer-Verlag, New York, 1988); J. Feder, *Fractals* (Plenum, New York, 1988).

[14] T. A. Hewett, in *Reservoir Characterization 2* (Society of Petroleum Engineers, Houston, TX, 1989).

[15] C. V. Deutch and A. C. Journel, *GSLIB: Geostatistical Software Library and User's Guide* (Oxford University Press, Oxford, UK, 1992).

[16] A. Tarantola, *Inverse Problem Theory, Methods for Data Fitting and Model Parameter Estimation* (Elsevier Science, Amsterdam, 1987).

[17] A. N. Tikhonov and V. Y. Arsenïn, *Solutions of Ill-posed Problems* (Halsted, New York, 1977).

[18] P. R. Ballin, A. G. Journel, and K. Aziz, J. Can. Pet. Technol. **31**, 52 (1992).

[19] P. Berest, N. Rakotomalala, J. P. Hulin, and D. Salin, Eur. Phys. J. A **6**, 309 (1999).

[20] R. Lenormand, Transp. Porous Media **18**, 245 (1995).